Asian Journal of Chemistry; Vol. 37, No. 10 (2025), 2514-2524
ASIAN JOURNAL OF CHEMISTRY
https://doi.org/10.14233/ajchem.2025.34414

Structural, Morphological, Optical and Magnetic Investigations of Pr^{3+}-Substituted Mn-Cd Spinel Ferrite Nanoparticles

M. DEVIKA[1], G. VINOD[2], MANDAVA VENKATA BASAVESWARA RAO[1,*] and P. BABY SUDHA LAKSHMI[3,*]

[1]Department of Chemistry, Krishna University, Machilipatnam-521004, India
[2]Department of Humanities & Sciences (Physics), Teegala Krishna Reddy Engineering College, Medbowli, Meerpet, Hyderabad-500097, India
[3]Department of Chemistry, Dr. M.R.A.R. College of P.G. Studies, Nuzvid-521201, India

*Corresponding authors: E-mail: vbrmandava@yahoo.com; dr.pbsl@gmail.com

Received: 6 July 2025 *Accepted*: 19 September 2025 *Published online*: 30 September 2025 AJC-22136

Spinel nano-ferrites offer a promising photocatalytic approach for environmental remediation. Employing a combustion method, a new spinel $Mn_{0.5}Cd_{0.5}Pr_xFe_{2-x}O_4$ (x = 0-5) nano-ferrite as photocatalysts have been developed for the degradation of Congo red dye. P-XRD, FTIR, HR-TEM, UV-VIS, VSM and photon-driven catalytic processes for the degradation of Congo red dye have been employed to analyze each of the $Mn_{0.5}Cd_{0.5}Pr_xFe_{2-x}O_4$ (x = 0-5) nano-ferrites. P-XRD analysis was used to determine the lattice strain and crystallite size of each nano-ferrite sample, revealing the crystallite sizes ranging from 23.11 to 32.84 nm. The total surface areas, densities, bond lengths and hopping lengths of each Pr-sample nanocrystal were also determined and calculated. FTIR analysis revealed two prominent frequency bands at 602 and 425 cm^{-1}, characteristic of spinel ferrites. The particle size and distribution of the nano-ferrites in the Pr-0 to Pr-5 samples were examined using FE-SEM, which showed spherical Pr-Mn-Cd nanoparticles with a tendency to aggregate. The direct allowed bandgap (E_g) values for Pr-0 through Pr-5 were estimated from Tauc plots as 2.66, 2.45, 2.34, 2.22, 2.10 and 1.97 eV, respectively. The variation in bandgap (E_g) values can be attributed to the combined effects of doping and particle size. Magnetic measurements showed a systematic decrease in saturation magnetization (M_s), magnetocrystalline anisotropy (K_1), coercivity (H_c) with Pr-substitution.

Keywords: Spinel ferrite nanoparticles, Pr-Mn-Cd ferrites, PL spectra, Soft magnet.

INTRODUCTION

The remarkable structural, magneto-optical, electrical properties and photocatalytic activity of spinel ferrite nanoparticles synthesized from various transition metal ions (Mn, Zn, Cd, Ni and Co) have made them a highly attractive class of nanomaterials in recent years [1,2]. Spinel ferrites based on transition metal ions set a new benchmark due to their unique and remarkable properties, enabling their use in a wide range of applications such as high-frequency devices, energy storage systems, transformers and microwave absorbers. Rare-earth (RE) soft magnets, such as those based on Nd-Fe-B and Sm-Co, have been the subject of a significant amount of research over the last ten years. However, the development of rare earth-free magnets has continually taken precedence in research due to the growing demand for high-performance soft magnets and the growing supply risk of rare earth strategic raw materials [3-5]. These magnets can nevertheless be used in applications where lesser performance is needed, even if their magnetism is weaker than that of compounds based on RE materials.

Photocatalysis is an eco-friendly process that uses light to generate electron-hole pairs, converting harmful organic pollutants into benign substances like CO_2 and H_2O [6-8]. Its advantages include high efficiency, low energy consumption, stability and versatility. Since only 4-5% of sunlight is UV, research focuses on developing visible-light-responsive photocatalysts to harness more solar energy [9,10]. Semiconductor photocatalysts are effective in degrading organic contaminants for environmental remediation. Magnetic semiconductor photocatalysts, such as spinel ferrites, also enable easy catalyst recovery from water, making them ideal for water treatment applications due to their excellent magnetic properties [11].

Manganese ferrite ($MnFe_2O_4$), a member of the spinel ferrite family, is a hard magnetic material with excellent properties such as high electrical resistivity, low coercivity and moderate saturation magnetization. Its exceptional chemical

stability and mechanical hardness make it suitable for harsh environments. $MnFe_2O_4$ has also proven effective in photocatalysis and can be easily recovered using an external magnetic field. Therefore, $Mn_{0.5}Cd_{0.5}Fe_2O_4$ was chosen as pristine sample for this study due to its outstanding characteristics. As reported by Akhtar *et al*. [12], although the incorporation of rare-earth (RE) cations in spinel ferrites is limited, the lattice offers significant potential for modifying their structural and physical properties. The 4*f*-electrons of RE cations shift the valence and conduction bands in spinel nano-ferrites, enhancing the visible light absorption. Similarly, cadmium ferrite ($CdFe_2O_4$), a soft magnetic material, is widely used as a photocatalyst for dye degradation due to its recyclability, narrow bandgap (1.2–2.4 eV) and chemical stability [13,14]. However, pure $CdFe_2O_4$ suffers from rapid electron-hole recombination under visible light, limiting its efficiency. Doping $CdFe_2O_4$ with additional elements, especially RE cations, improves photocatalytic performance as RE ions preferentially occupy octahedral sites due to their larger ionic radius, enhancing light absorption and degradation. Yet, the ionic radius difference between Fe and RE ions restricts RE solubility and doping levels in the spinel lattice. Nonetheless, appropriate RE^{3+} doping can significantly modify the physical properties of these ferrites [15-20]. The unique electrical configuration of $4f^1 5s^2 5p^6$ distinguishes praseodymium from other rare earth elements [21]. The presence of praseodymium in the ferrite matrix may influence the interaction between 4*f* and 3*d* orbitals. This study focuses on the effect of Pr^{3+} doping on Mn-Cd ferrite nanoparticles, a topic not reported in the literature. The main objective is to synthesize the smallest possible ferrite nanoparticles using the new formula ($x \leq 0.01$, step 0.05) and to investigate the effect of Pr^{3+} ions on their structural, optical, spectral and soft magnetic properties.

EXPERIMENTAL

Synthesis of spinal ferrites: The starting materials were used in the citrate combustion method to synthesize praseodymium-substituted manganese-cadmium ferrites having general formula $Mn_{0.5}Cd_{0.5}Pr_xFe_{2-x}O_4$, where $0.0 \leq x \leq 0.05$: citric acid, $Mn(NO_3)_2{\cdot}6H_2O$, $Cd(NO_3)_2{\cdot}6H_2O$, $Fe(NO_3)_3{\cdot}6H_2O$ and $Pr(NO_3)_3{\cdot}9H_2O$. The metal nitrates were mixed in stoichiometric ratios in ethylene glycol, continuously stirred and heated to 250 ºC until powder formation [22]. To accelerate the process, ammonia was gradually added to the metal nitrate and citric acid solution until the pH reached 7 [23]. The mixture was then heated on a hot plate at 250 ºC until it gelled, produced dense smoke and underwent self-sustained combustion. The resulting $Mn_{0.5}Cd_{0.5}Pr_xFe_{2-x}O_4$ samples (labeled as Pr-0 to Pr-5) were converted into ash. The powders were collected, ground and prepared for further analysis.

Characterization: This work employed several kinds of techniques to obtain a better understanding of the physical characteristics of nano-ferrite $Mn_{0.5}Cd_{0.5}Pr_xFe_{2-x}O_4$ samples. The Shimadzu P-XRD 6000 diffractometer was utilized to analyze X-ray diffraction (P-XRD) peaks using a radiation source with a wavelength of Cu*K*α (λ = 0.15405 nm). The infrared (IR) absorption characteristics of the Pr-Mn-Cd samples were investigated in the wavenumber range of 1000-200 cm^{-1} using a Perkin-Elmer 1430 spectrometer. The surface morphology of $Mn_{0.5}Cd_{0.5}Pr_xFe_{2-x}O_4$ nano-ferrites was analyzed using field emission scanning electron microscopy (FE-SEM). After dispersion in DMF, UV–Vis absorption spectra were recorded in the 200-1000 nm range using a UVS-2800 spectrophotometer. Photoluminescence (PL) emission and excitation spectra were measured with an Edinburgh Instruments FS920 spectrometer equipped with a 450 W Xe lamp. Magnetic properties, including anisotropy constant, initial permeability and magnetic moment, were evaluated using a Lakeshore 7410 vibrating sample magnetometer (VSM) under a 20 kOe field at room temperature (300 K).

RESULTS AND DISCUSSION

XRD studies: The synthesized $Mn_{0.5}Cd_{0.5}Pr_xFe_{2-x}O_4$ nano-ferrites were analyzed using P-XRD, with Pr^{3+} concentration varied from $x = 0.00$ to 0.05 in additions of 0.010. As shown in Fig. 1, the diffraction patterns of the ferrite samples exhibit distinct peaks corresponding to the (111), (220), (311), (222), (400), (511), (440) and (533) crystallographic planes, confirming the spinel structure. These peaks strongly indicate the formation of homogeneous single-phase products, as they closely match the standard diffraction patterns of $MnFe_2O_4$ (JCPDS card no. 74-2403) and $CdFe_2O_4$ (JCPDS card no. 22-1086). No impurities were detected in the $Mn_{0.5}Cd_{0.5}Pr_xFe_{2-x}O_4$ samples ($x = 0$ to 5), regardless of Pr^{3+} content [24,25]. These findings confirm the successful synthesis of single-phase nano-ferrites, indicating that Pr^{3+} ions effectively substituted Fe^{3+} without disrupting the cubic symmetry of the host lattice. Both doped and undoped samples exhibited high purity [26].

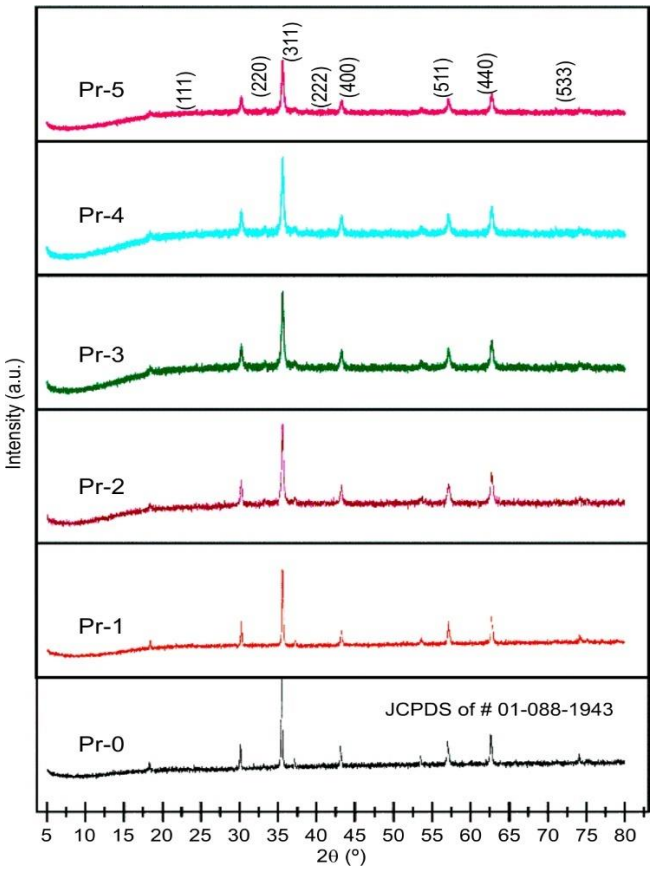

Fig. 1. P-XRD patterns of $Mn_{0.5}Cd_{0.5}Pr_xFe_{2-x}O_4$; x = Pr-0 to Pr-1 nano-ferrites

Table-1 presents the structural parameters derived from the analysis and Fig. 1 illustrates the shift in the angular position of the prominent (311) diffraction peak. As Pr^{3+} substitution increased from Pr-0 to Pr-5, the 2θ value for the (311) plane generally decreased from 35.878º to 35.831º, indicating slight lattice expansion. This shift suggests that Pr^{3+} ions are incorporated into the ferrite lattice, likely occupying interstitial or substitutional sites, leading to structural distortions and changes in interplanar spacing. The observed peak shift corresponds to the introduction of tensile strain, which increases the interplanar distance, which is consistent with the strain data.

The average crystallite size (D) was determined using Scherrer's equation [27] and the most prominent (311) peak. Moreover, the other structural parameters such as the lattice parameter, cell value, X-ray density, bulk density and porosity of fabricated samples were also determined [28,29].

$$D_{P\text{-}XRD}\ (nm) = \frac{k\lambda}{\beta \cos\theta} \quad (1)$$

According to the Scherrer equation (eqn. 1), the crystallite size increases gradually as the Pr^{3+} level rises, extending from 23.11 nm for the undoped sample (Pr-0) to 32.841 nm for Pr-5. The presence of rare-earth ions may improve grain growth by acting as growth promoters all over the synthesis process, which could explain this increase in the crystallite size. The magnetic characteristics can be determined from the hopping lengths (L_A and L_B), demonstrating the separation between magnetic ions in the tetrahedral (A) and octahedral (B) sites. As *x* grows from Pr-0 to Pr-5, the hopping lengths L_A and L_B exhibit a small increase, rising from 3.5943 Å to 3.6026 Å and 2.9415 Å to 2.9480 Å, respectively. The lattice expansion seen in the P-XRD analysis, where the substitution of more expansive Pr^{3+} ions corresponds to an overall enhancement of lattice parameters, which is consistent with this increase in hopping lengths [28,30,31]. The super-exchange interactions that give the ferrite system its magnetic characteristics can be influenced by the increased distances between the magnetic ions caused by the lattice's expansion. The magnetic ordering temperature and total magnetization of the material may be impacted by the weaker super-exchange interactions, which are generally produced through longer hopping lengths. Table-2 shows the value of lattice constant (a) which was improved from 8.4351 Å to 8.4497 Å. As ions Pr^{3+} have greater ionic radius (1.14 Å) as compared to Fe^{3+} ion (0.69 Å), Therefore, this increase is attributed due to the substitution of Pr^{3+} ions. The incorporation of Pr^{3+} ions into the cubic structure of $Mn_{0.5}Cd_{0.5}Fe_{2-x}Pr_xO_4$ nano-ferrites contributes to the structural stabilization by integrating Pr^{3+} ions into the crystal lattice [32].

As shown in Table-2, the X-ray density (d_x) of the nano-spinel ferrites increases with rising Pr^{3+} content, from 5.9451 g/cm^3 (Pr-0) to 5.9859 g/cm^3 (Pr-5). This increase is attributed to the substitution of lighter Fe^{3+} ions (atomic weight 55.85 g/mol) with heavier Pr^{3+} ions (atomic weight 59.675 g/mol) [33]. Similarly, the bulk density (d_B) shows a slight rise from 2.435 g/cm^3 to 3.164 g/cm^3. However, the prominent difference between d_x and d_B suggests the presence of porosity in the samples, which may affect overall densification. Calculated porosity (P) increases from 47.47% to 59.32% with higher Pr^{3+} substitution, likely due to the lattice distortion and looser packing caused by the larger ionic radius of Pr^{3+} ions [34].

Mechanical parameters of nano-spinal ferrites: P-XRD data is used to estimate mechanical parameters such as crystallite size, microstrain, dislocation density and specific surface area, providing insight into the microstructural quality of the material [35,36]. As Pr^{3+} concentrations increase, the specific surface area (S) decreases from Pr-0-43.1017 m^2/g for Pr-5-30.5260 m^2/g. P-XRD and strain studies have verified that the increase in grains linked to the growing crystallite size is most

TABLE-1
DETAILS OF STOICHIOMETRIC CONCENTRATIONS OF PRECURSORS REQUIRED FOR THE Pr-DOPED Mn-Cd NANO-FERRITES SYNTHESIS

Composition	$Mn_{0.5}Cd_{0.5}Fe_2O_4$	$Mn_{0.5}Cd_{0.5}Fe_{1.99}Pr\text{-}0_{.010}O_4$	$Mn_{0.5}Cd_{0.5}Fe_{1.98}Pr\text{-}0_{.020}O_4$	$Mn_{0.5}Cd_{0.5}Fe_{1.97}Pr\text{-}0_{.030}O_4$	$Mn_{0.5}Cd_{0.5}Fe_{1.96}Pr\text{-}0_{.040}O_4$	$Mn_{0.5}Cd_{0.5}Fe_{1.985}Pr\text{-}0_{.050}O_4$
Molecular weight	259.3301	259.3640	259.4050	259.4351	259.4608	259.5010
$Mn(NO_3)_2{\cdot}6H_2O$ g/mol	11.2992	11.2160	11.1340	11.0532	10.9736	10.8951
$Cd\ NO_3)_2{\cdot}6H_2O$ g/mol	1.08214	1.07417	1.06632	1.05858	1.05095	1.04343
$Pr\ (NO_3)_3.5H_2O$ g/mol	–	0.2822	0.5603	0.8344	1.1045	1.3708
$Fe\ (NO_3)_3.9H_2O$ g/mol	34.1004	33.5954	33.0978	32.6074	32.1240	31.6476
$C_6H_8O_7{\cdot}H_2O$ g/mol	26.6059	26.4100	26.2169	26.0266	25.8391	25.6542

TABLE-2
STRUCTURAL AND PHYSICO-CHEMICAL PARAMETERS OF SYNTHESIZED $Mn_{0.5}Cd_{0.5}Pr_xFe_{2-x}O_4$ (x = 0 to 4) NANO-FERRITES

x	Pr-0	Pr-1	Pr-2	Pr-3	Pr-4	Pr-5
FWHM	0.3614	0.2991	0.2963	0.2833	0.2708	0.2543
d spacing (nm)	2.5356	2.5383	2.5391	2.5393	2.5398	2.54
D (nm)	23.11	27.91	28.18	29.47	30.83	32.84
a (Å)	8.4351	8.444	8.4466	8.4474	8.449	8.4497
V (Å)^3	571.93	578.1	577.968	577.267	576.94	575.914
L_A	3.5943	3.6072	3.6069	3.6055	3.6048	3.6026
L_B	2.9348	2.9453	2.945	2.9438	2.9433	2.9415
d_x (g/cm^3)	5.9451	5.9599	5.9623	5.9706	5.9744	5.9859
d_B (g/cm^3)	3.164	2.833	2.745	2.67	2.628	2.435
P (%)	47.47	52.47	53.96	55.28	56.01	59.32

likely the cause of this drop in specific surface area (Table-3). Reduced specific surface area values result from a decrease in surface area per unit mass as crystallite size increases. This trend is expected, as larger grains possess fewer grain boundaries, which are significant contributors to the overall surface area [37].

TABLE-3
MECHANICAL PARAMETERS OF $Mn_{0.5}Cd_{0.5}Pr_xFe_{2-x}O_4$ (x = 0 to 4) NANO-FERRITE DERIVED FROM STRUCTURAL DATA

Composition	Specific surface area (m^2/g)	Packing factor (P)	Strain (ε)	Dislocation density (g/m^3)
Pr-0	43.1017	9.2618	0.1606	0.1163
Pr-1	36.0712	11.1452	0.1595	0.1147
Pr-2	35.7128	11.2534	0.1595	0.1147
Pr-3	34.1019	11.7734	0.1596	0.1149
Pr-4	32.5736	12.3202	0.1597	0.1150
Pr-5	30.5260	13.1292	0.1599	0.1152

FESEM-EDS analysis: Fig. 2 shows FESEM images of the prepared $Mn_{0.5}Cd_{0.5}Pr_xFeO_4$ (x = 0 to 5) nanoferrites. The grains exhibit an irregular distribution and predominantly the spherical morphology. The agglomeration observed may be attributed to the strong interactions between magnetic nanoparticles and their high surface energy at small sizes. The particle diameters of the Pr-substituted nano-ferrites range from approximately 25 to 35 nm. The presence of larger Pr^{3+} ionic radii likely contributes to the formation of smoother, more uniform structures and a reduction in particle size.

Moreover, Pr^{3+} ions also influence the microstructural evolution in two distinct ways: half of the ions accumulate at grain boundaries, introducing disturbances that hinder grain growth, while the remaining ions induce internal lattice stress and distortion. As illustrated in Fig. 2, the incorporation of Pr^{3+} ions promotes an insulating effect, leading to the formation of well-connected fine grains [38]. This results in a reduced number of charge carriers (holes) and contributes to a more ordered and homogeneous microstructure.

Fig. 3 presents the particle size distribution histograms for $Mn_{0.5}Cd_{0.5}Pr_xFeO_4$ (x = 0 to 5) nanoferrites. The observed ferromagnetic behaviour in the synthesized Mn-Cd nanoferrites is primarily attributed to their particulate nature and aligned spin structure. In materials science, a single particle may comprise multiple grains. In this study, the introduction of a dopant significantly influenced particle size and composition, although the overall morphology remained unaffected. Notably, increased grain size correlates with enhanced domain wall formation, which requires greater energy for wall motion compared to the domain rotation during magnetization and demagnetization processes [39].

Elemental composition was assessed using EDS as shown in Fig. 4. Only the characteristic peaks corresponding to Mn, Cd, Pr, Fe and O were detected, confirming the chemical purity of all synthesized nanoferrites. The stoichiometric ratios of the elements matched the initial precursor concentrations. A quantitative EDS analysis was performed for all $Mn_{0.5}Cd_{0.5}Pr_xFeO_4$ (x = 0 to 5) nano-spinel ferrites, with the results summarized in Table-4. Due to the low atomic weight and small ionic radius, Pr in samples Pr-1 and Pr-2 was not distinctly detected in the EDS spectra. Additionally, the increase in atomic percentages of Pr and O is associated with the formation of the (311) Miller index phase shift, which enhances their X-ray signal intensity in the EDS analysis.

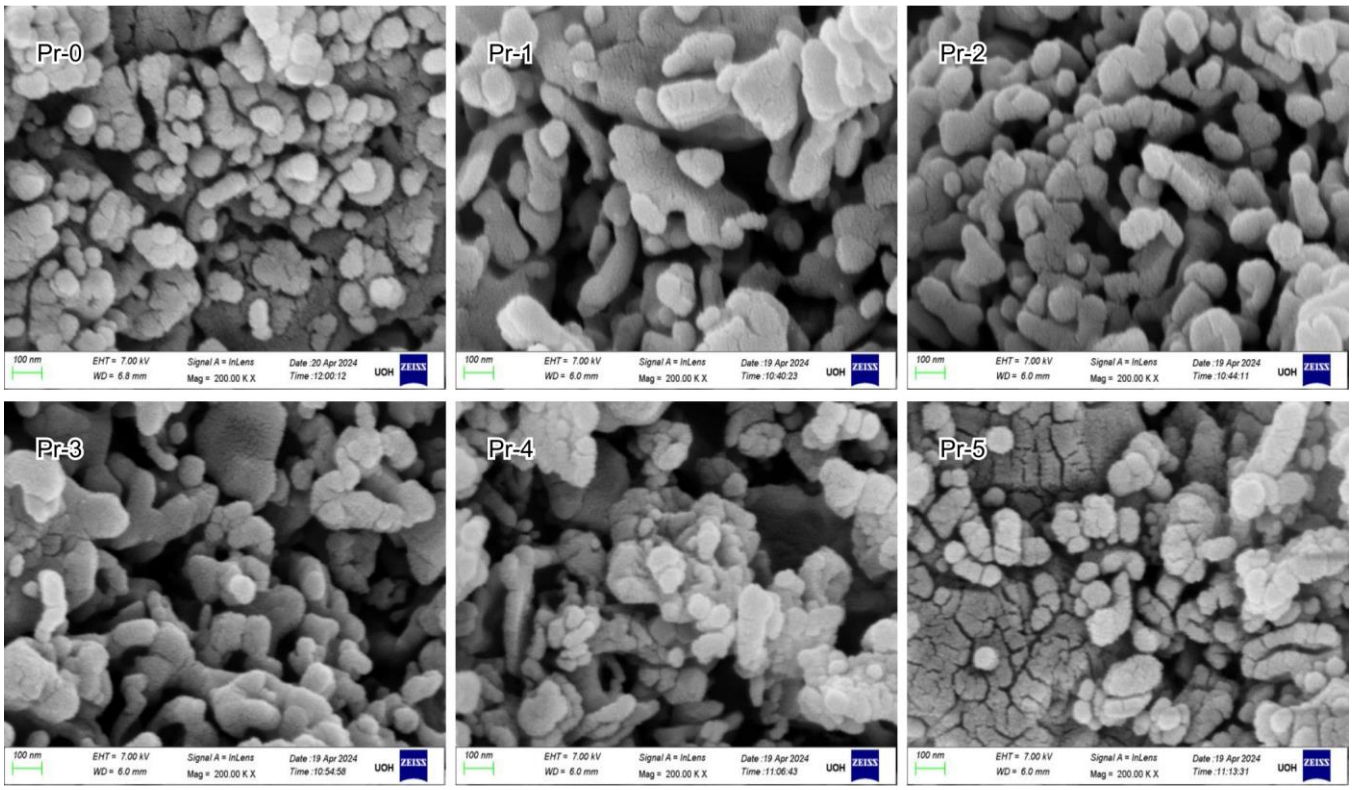

Fig. 2. FE-SEM images of different samples: Pure Pr-0 to Pr-5 ferrite samples

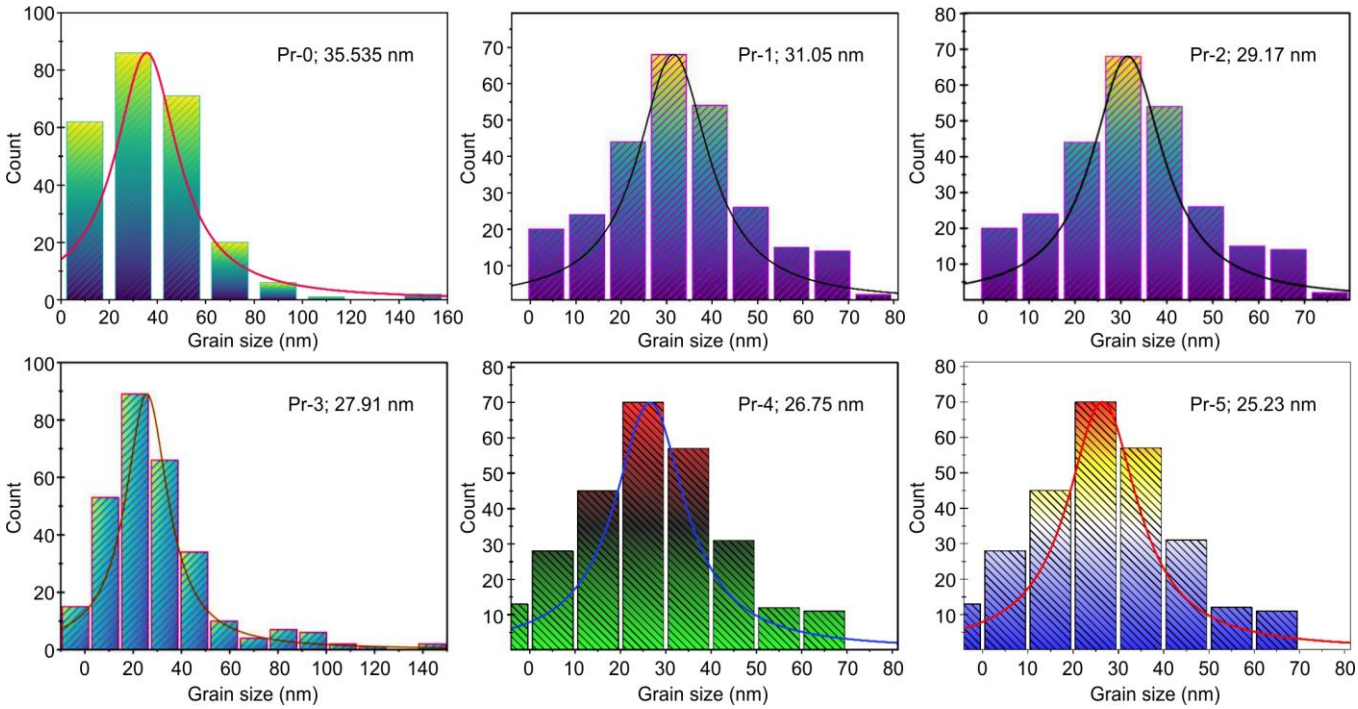

Fig. 3. Histograms for grain size calculation of $Mn_{0.5}Cd_{0.5}Pr_xFe_{2-x}O_4$; x = Pr-0 to Pr-1 nano-ferrites

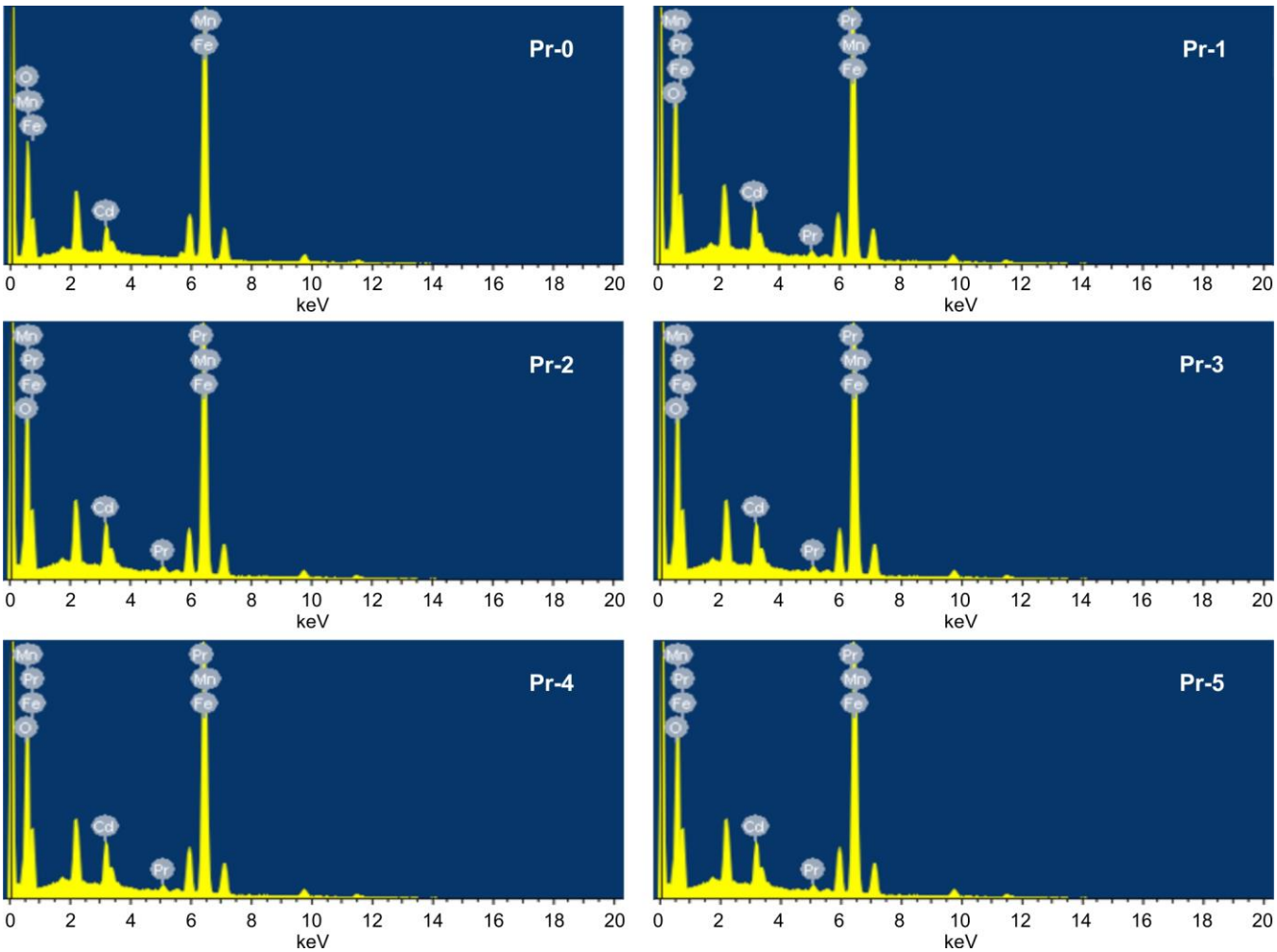

Fig. 4. EDS images of synthesized ($Mn_{0.5}Cd_{0.5}Pr_xFe_{2-x}O_4$; x = Pr-0 to Pr-5) nano-ferrites

TABLE-4
ELEMENTAL AND ATOMIC PERCENTAGES OF ELEMENTS IN $Mn_{0.5}Cd_{0.5}Pr_xFe_{2-x}O_4$ (x = 0 to 4) NANO-FERRITES

Element (Pr-0)	Weight (%)	Atomic (%)	Element (Pr-1)	Weight (%)	Atomic (%)	Element (Pr-2)	Weight (%)	Atomic (%)
O K	20.77	48.77	O K	21.84	49.91	O K	21.84	49.91
Mn K	10.04	6.87	Mn K	8.83	5.88	Mn K	8.83	5.88
Fe K	62.71	42.19	Fe K	65.8	43.07	Fe K	65.8	43.07
Cd L	6.48	2.16	Cd L	3.53	1.15	Cd L	3.53	1.15
			Pr L	0	0	Pr L	0	0
Totals	100		Totals	100		Totals	100	
Element (Pr-3)	Weight (%)	Atomic (%)	Element (Pr-4)	Weight (%)	Atomic (%)	Element (Pr-5)	Weight (%)	Atomic (%)
O K	25.63	56.15	O K	25.63	56.15	O K	21.61	50.74
Mn K	8.66	5.52	Mn K	8.66	5.52	Mn K	9	6.15
Fe K	56.64	35.55	Fe K	56.64	35.55	Fe K	59.28	39.88
Cd L	8.14	2.54	Cd L	8.14	2.54	Cd L	7.96	2.66
Pr L	0.94	0.23	Pr L	0.94	0.23	Pr L	2.16	0.58
Totals	100		Totals	100		Totals	100	

HR-TEM analysis: TEM images of $Mn_{0.5}Cd_{0.5}Pr_xFe_{2-x}O_4$; ($x$ = 0 to 5) nanoferrites exhibit a uniform spherical morphology, as confirmed by FE-SEM micrographs (Fig. 5). To determine the physico-chemical properties of the nano-ferrites, particle size distribution was analyzed using ImageJ software by evaluating over 200 particles per sample (Fig. 5). The crystalline nature of the samples is evidenced by clear lattice fringes with interplanar spacings of 0.251 nm and 0.650 nm for Pr-0, 0.653 nm and 0.254 nm for Pr-3 and 0.654 nm and 0.250 nm for Pr-5. These spacings correspond to the (311) and (422) planes of the spinel structure, respectively. The results showed good agreement with P-XRD and TEM measurements, with particle sizes decreasing from 32.10 nm to 26.55 nm as the Pr^{3+} doping level increased from Pr-0 to Pr-5. HRTEM images of Pr-Mn-Cd nanoparticles (Fig. 5b) also show distinct lattice fringes associated with the same atomic planes, confirming their well-defined crystalline structure [40]. Furthermore, selected area electron diffraction (SAED) patterns for both undoped and Pr-doped samples (Fig. 6) display ring patterns indicative of polycrystalline nature. These HRTEM and SAED results are consistent with the findings from P-XRD analysis.

FTIR analysis: The characteristic infrared bands at in the 602-415 cm^{-1} range correspond to the metal–oxygen vibrational modes typical of spinel ferrites, originating from two distinct sub-lattices: the tetrahedral (A) and octahedral (B) sites, as shown in Table-5.

Fig. 7 shows the FTIR spectra of $Mn_{0.5}Cd_{0.5}Pr_xFe_{2-x}O_4$ (x = 0 to 5) nanoferrites within the 1000-390 cm^{-1} far-infrared region. All nano-spinel ferrite samples exhibit two distinct

TABLE-5
KEY IR VIBRATIONAL BANDS AND BAND GAP (E_g) VALUES OF Pr-DOPED Mn-Cd NANO-FERRITES

x	Vibrational modes (ν_1)	Vibrational modes (ν_2)	Bandgap energy (E_g)
Pr-0	588	415	2.66
Pr-1	591	417	2.45
Pr-2	594	420	2.34
Pr-3	597	422	2.22
Pr-4	599	423	2.10
Pr-5	602	425	1.97

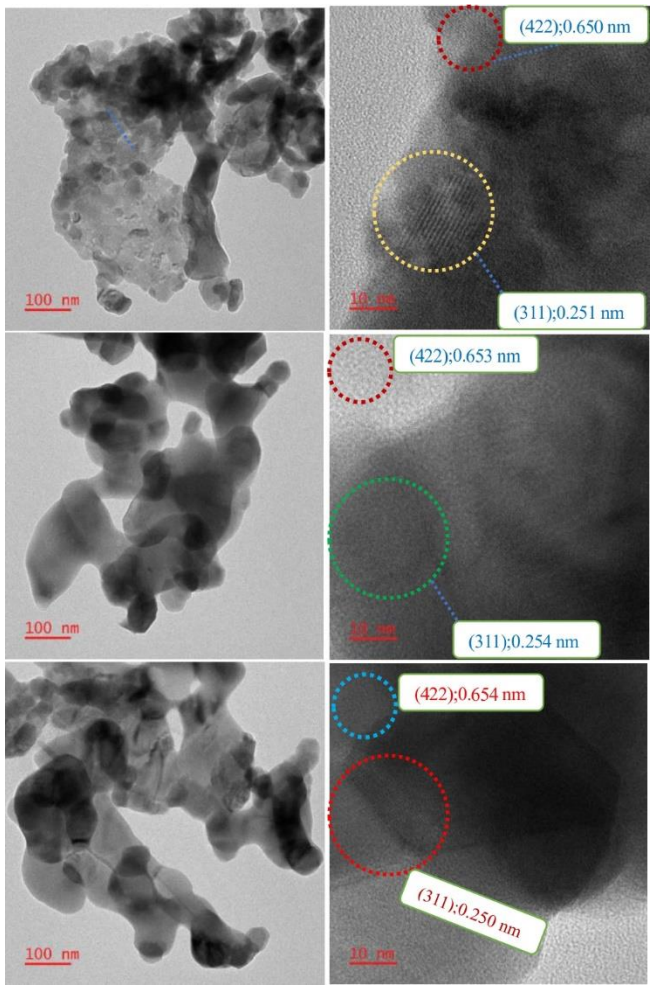

Fig. 5. TEM and HR-TEM images of as-synthesized representative $Mn_{0.5}Cd_{0.5}Pr_xFe_{2-x}O_4$ ferrite samples Pr-0, Pr-3 and Pr-5, respectively

M–O vibrational modes, ν_1 and ν_2, which correspond to the characteristic infrared bands. The second band (ν_2: 602-588 cm^{-1}) is attributed to the vibrations of trivalent metal ions bonded to oxygen in the tetrahedral (A-site) coordination, whereas the first band (ν_1: 425–415 cm^{-1}) is associated with the stretc-

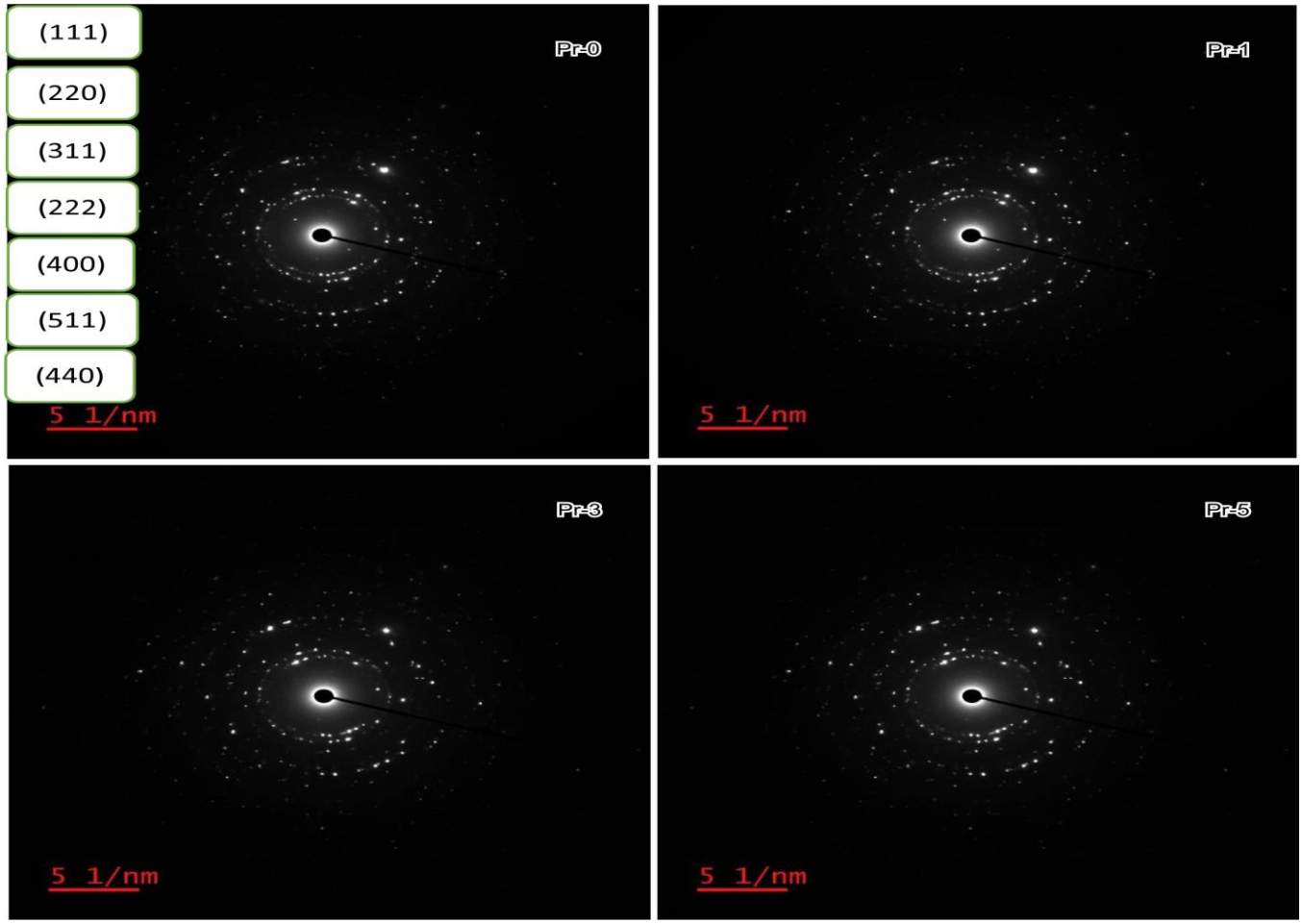

Fig. 6. SAED images of as-synthesized representative $Mn_{0.5}Cd_{0.5}Pr_xFe_{2-x}O_4$ ferrite samples Pr-0, Pr-3 and Pr-5, respectively

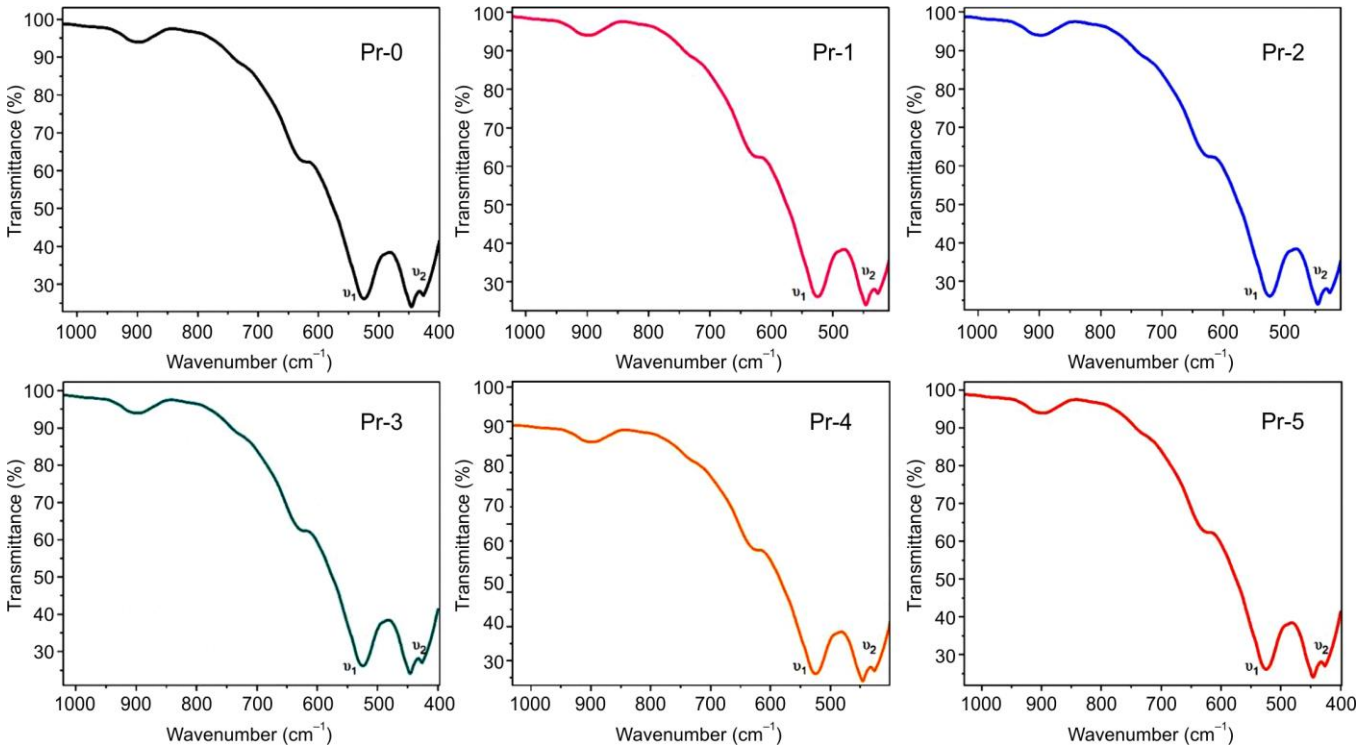

Fig. 7. FTIR spectra of all $Mn_{0.5}Cd_{0.5}Pr_xFe_{2-x}O_4$; x = Pr-0 to Pr-5 nanomaterials

hing vibrations of metal ions (Cd^{2+}, Mn^{2+} or Fe^{3+}) in the octahedral (B-site) environments [41]. The presence of both ν_1 and ν_2 modes confirms the successful formation of the $Mn_{0.5}Cd_{0.5}Pr_xFe_{2-x}O_4$ spinel nanoferrite phase *via* the sol-gel synthesis route [42].

UV-VIS analysis: The optical behaviour and bandgap energy (E_g) variation of $Mn_{0.5}Cd_{0.5}Pr_xFe_{2-x}O_4$ (x = 0 to 5) nano-ferrites were investigated using a UV-Vis spectrophotometer in the 300-800 nm wavelength range. The absorbance spectra of Pr^{3+}-doped Mn-Cd ferrites samples are presented in Fig. 8. As shown, the absorption intensity is highest at shorter wavelengths and gradually decreases with increasing wavelength, approaching near-zero absorption as saturation is reached. The optical bandgap of the nanomaterials was determined using Tauc's method [43-46]:

$$(\alpha h\nu)^n = A\,(h\nu - E_g) \quad (1)$$

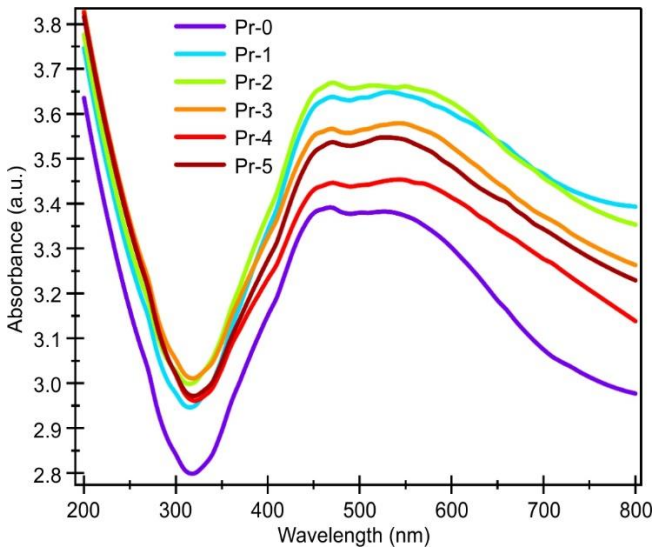

Fig. 8. UV–Vis absorbance spectra for $Mn_{0.5}Cd_{0.5}Pr_xFe_{2-x}O_4$; x = Pr-0 to Pr-5 nanoferrites

The Tauc plots for all $Mn_{0.5}Cd_{0.5}Pr_xFe_{2-x}O_4$ (x = 0 to 5) samples are shown in Fig. 9. Bandgap energies (E_g) were estimated by extrapolating the linear portion of the plot to the x-axis and the calculated values are listed in Table-5. As shown, the bandgap gradually decreases from 2.66 eV for the undoped sample to 1.97 eV with increasing Pr^{3+} doping. The higher bandgap in the undoped Mn-Cd ferrite is attributed to orbital interactions between O^{2-} 2*p* and Fe^{3+} 3*d* states. Upon Pr^{3+} doping, the appearance of Pr^{3+} 4*f* states just below the conduction band introduces new energy levels, reducing the bandgap. This reduction is due to charge transfer from the Pr^{3+} 4*f*-states to the conduction band, facilitated by their interaction with the O^{2-} 2*p* valence band orbitals [47]. A similar study by Somvanshi *et al*. [48] on Zn-Mg ferrites using diffuse reflectance spectroscopy reported the bandgap values ranging from 2.66 to 1.97 eV, consistent with the trend observed in the present work, though the minimum value reported here is slightly lower.

VSM analysis: The magnetic characteristics of ferrites are produced through the cations at the tetrahedral site (A) and octahedral site (B). Trivalent metal cations in conventional

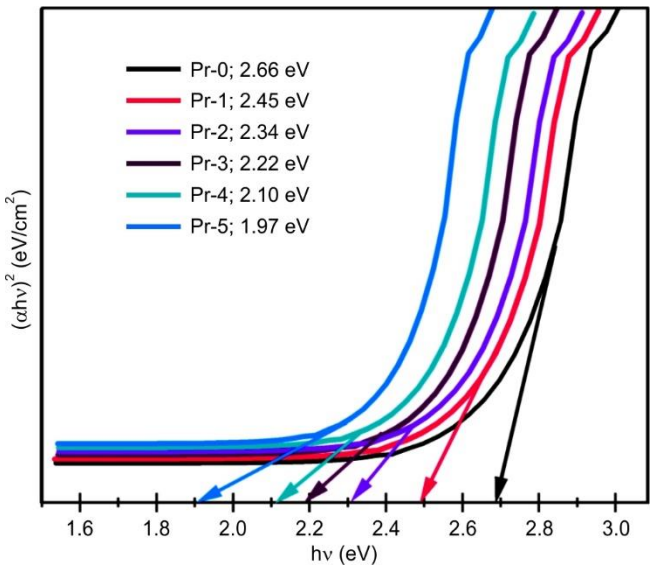

Fig. 9. Tauc plots for $Mn_{0.5}Cd_{0.5}Pr_xFe_{2-x}O_4$; x = Pr-0 to Pr-5 nano-ferrites

spinel nanoferrites tend to occupy octahedral positions, while bivalent metal cations occupy tetrahedral positions. The net magnetization in nano-ferrites primarily arises from the B-site, which possesses a higher magnetic moment compared to the A-site. Fig. 10 displays the magnetic hysteresis loops of $Mn_{0.5}Cd_{0.5}Pr_xFe_{2-x}O_4$ (x = 0 to 5) nanoferrites recorded at room temperature.

Table-6 provides a summary of key parameters such as coercivity (H_c), magnetic moment (n_B), squareness ratio (M_r/M_s), remanent magnetization (M_r), saturation magnetization (M_s) and anisotropy constant (K). As Pr^{3+} concentrations increased, a decrease in saturation magnetization was observed. Magnetization in $Mn_{0.5}Cd_{0.5}Pr_xFe_{2-x}O_4$ (x = 0 to 5) nanoferrites depends on the distribution of ions between tetrahedral (A) and octahedral (B) sites. Increasing Pr^{3+} content causes Fe^{3+} ions to shift from B to A sites, while Mn^{2+} ions occupy both. Saturation magnetization (M_s) decreases with higher Pr doping, as Pr^{3+} preferentially occupies B sites, weakening magnetic interactions, consistent with prior studies [49].

Coercivity initially increases due to the uniform cation distribution and high anisotropy but then decreases with further doping, correlating with reduced crystallite size and squareness ratio (Table-6). The highest coercivity occurs at Pr-5, attributed to its small particle size, high anisotropy and cation distribution. Squareness ratios below 0.10 indicate paramagnetic behaviour, while values above 1.0 at Pr-0 and Pr-5 suggest ferromagnetism [50]. Table-6 also presents the synthesized spinel nanoferrites computed initial permeability magnetic moment and anisotropy constants.

Conclusion

In this work, Pr^{3+}-substituted Mn-Cd spinel nanoferrites were successfully synthesized using the sol-gel technique. The crystalline sizes of the prepared spinel nanoferrites ranged from 23.11 to 32.84 nm and the P-XRD tests suggested a cubic spinel structure having developed. HR-TEM and FE-SEM images showed spherically formed and uniform nanoparticles. Furthermore, EDS analysis confirmed the elemental composition with no detectable impurities, corroborating the P-XRD

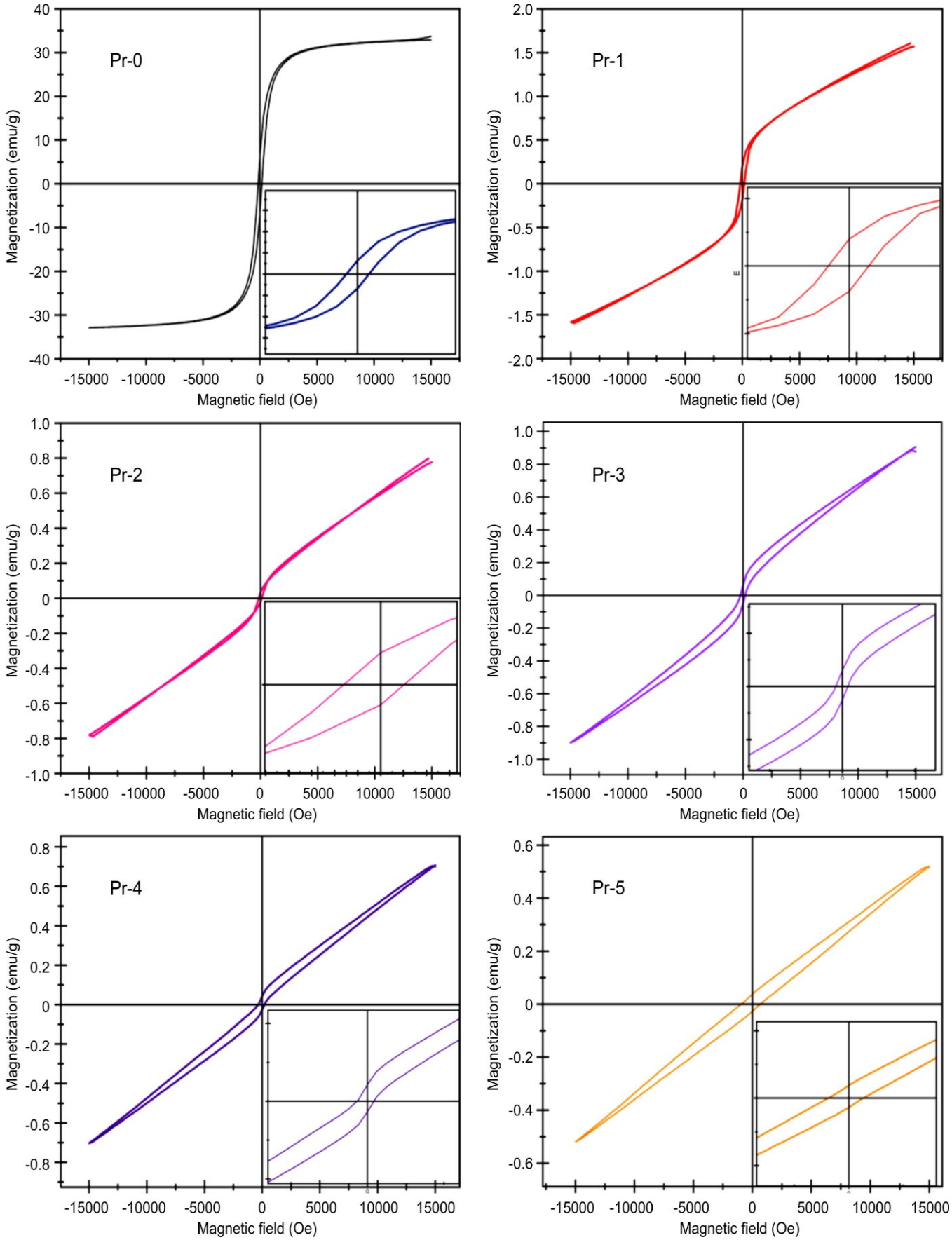

Fig. 10. M- H loop of synthesized $Mn_{0.5}Cd_{0.5}Pr_xFe_{2-x}O_4$; *x* = Pr-0 to Pr-5 nanoparticles

TABLE-6
MAGNETIC PROPERTIES DATA INCLUDING SATURATION MAGNETIZATION, REMANENCE AND COERCIVITY OF Pr-DOPED Mn-Cd NANO-FERRITES

x	M_s (emu/g)	M_r (emu/g)	M_r/M_s (emu/g)	HC (Oe)	Anisotropy constant (K)	Initial permeability (μ_i)	Magnetic moment n_B
Pr-0	28.045	6.0365	0.215	194.554	6.9372	2620.1498	1.3022
Pr-1	1.5645	0.2056	0.131	180.336	115.2675	0.5927	0.0727
Pr-2	0.7863	0.0745	0.095	211.678	269.2077	0.0647	0.0365
Pr-3	0.8891	0.0542	0.061	232.117	261.0696	0.0892	0.0413
Pr-4	0.6901	0.0437	0.063	274.452	397.6989	0.0369	0.0321
Pr-5	0.5134	0.0385	0.075	384.675	749.2696	0.0116	0.0239

results. These findings indicate that Pr^{3+}-doped Mn-Cd nanoferrites exhibit enhanced magnetic properties, making them promising candidates for magnetic filters, storage devices, and other magnetic applications. The maximum saturation magnetization (M_s) of $Mn_{0.5}Cd_{0.5}Pr_xFe_{2-x}O_4$ (x = 0 to 5) nanoferrites reached 28.045 emu/g, which significantly decreased to approximately 0.5134 emu/g for the highest doped Pr^{3+} (Pr-5). This reduction in M_s, along with decreased coercivity and remanence, is attributed to the lower magnetic moment of Pr^{3+} ions compared to Fe ions.

ACKNOWLEDGEMENTS

One of the authors, GV, gratefully acknowledges the financial support received from Council of Scientific & Industrial Research (CSIR-HRDG), Government of India, New Delhi, India (Ref. no. 09/132(0879)/2018 EMR-I).

CONFLICT OF INTEREST

The authors declare that there is no conflict of interests regarding the publication of this article.

REFERENCES

1. F. Hirosawa and T. Iwasaki, *Solid State Sci.*, **118**, 106655 (2021); https://doi.org/10.1016/j.solidstatesciences.2021.106655
2. A. Mills and S. Le Hunte, *J. Photochem. Photobiol. Chem.*, **108**, 1 (1997); https://doi.org/10.1016/S1010-6030(97)00118-4
3. J. Patel, K. Parekh and R.V. Upadhyay, *Int. J. Therm. Sci.*, **114**, 64 (2017); https://doi.org/10.1016/j.ijthermalsci.2016.12.011
4. X. Qin, H. Zhang, F. Wang, Y. Ma and X. Xu, *J. Mater. Sci.*, **59**, 10182 (2024); https://doi.org/10.1007/s10853-024-09797-w
5. M. Grigoras, M. Lostun, M. Urse, F. Borza, H. Chiriac and N. Lupu, *J. Magn. Magn. Mater.*, **447**, 68 (2018); https://doi.org/10.1016/j.jmmm.2017.09.059
6. F.S. Arghavan, T.J. Al-Musawi, E. Allahyari, M.H. Moslehi, N. Nasseh and A. Hossein Panahi, *Mater. Sci. Semicond. Process.*, **128**, 105725 (2021); https://doi.org/10.1016/j.mssp.2021.105725
7. M.A. Bajiri, A. Hezam, K. Namratha, B.M. Al-Maswari, H.S. Bhojya Naik, K. Byrappa, N. Al-Zaqri, A. Alsalme and R. Alasmari, *New J. Chem.*, **45**, 13499 (2021); https://doi.org/10.1039/D1NJ01044A
8. M.A. Bajiri, A. Hezam, K. Namratha, R. Viswanath, Q.A. Drmosh, H.S. Bhojya Naik and K. Byrappa, *J. Environ. Chem. Eng.*, **7**, 103412 (2019); https://doi.org/10.1016/j.jece.2019.103412
9. S. Alkaykh, A. Mbarek and E.E. Ali-Shattle, *Heliyon*, **6**, e03663 (2020); https://doi.org/10.1016/j.heliyon.2020.e03663
10. G. Vishnu, S. Singh, T.S.S. Kumar Naik, P.C. Ramamurthy, H.S. Bhojya Naik, R. Viswanath, P. Bhadrecha, J. Singh, N.A. Khan and S. Zahmatkesh, *J. Clean. Prod.*, **404**, 136977 (2023); https://doi.org/10.1016/j.jclepro.2023.136977
11. A.A. Alghamdi, M.S. Sadeq, E. Abdel-Fattah, M.A.Z. Qutub and M.A. Abdo, *Opt. Mater.*, **155**, 115904 (2024); https://doi.org/10.1016/j.optmat.2024.115904
12. P. Akhtar, M.N. Akhtar, M.A. Baqir, A. Ahmad, M.U. Khallidoon, M. Farhan and M.A. Khan, *J. Mater. Sci. Mater. Electron.*, **32**, 7692 (2021); https://doi.org/10.1007/s10854-021-05487-4
13. S.P. Dalawai, T.J. Shinde, A.B. Gadkari and P.N. Vasambekar, *Bull. Mater. Sci.*, **36**, 919 (2013); https://doi.org/10.1007/s12034-013-0529-1
14. N. Amin, A. Razaq, A.U. Rehman, K. Hussain, M.A.U. Nabi, N.A. Morley, M. Amami, A. Bibi, M.I. Arshad, K. Mahmood, M. Fatima, M. Akhtar, S. Akbar, A. Manzoor, H.T. Ali, M. Yusuf and S. Amin, *J. Supercond. Nov. Magn.*, **34**, 2945 (2021); https://doi.org/10.1007/s10948-021-06053-z
15. B. Zheng, J. Fan, B. Chen, X. Qin, J. Wang, F. Wang, R. Deng and X. Liu, *Chem. Rev.*, **122**, 5519 (2022); https://doi.org/10.1021/acs.chemrev.1c00644
16. M. Rostami, R.M. Zamani, K.M. Aghajanzadeh and H. Danafar, *J. Pharm. Investig.*, **48**, 657 (2018); https://doi.org/10.1007/s40005-017-0362-4
17. N. Masunga, V.S. Vallabhapurapu and B.B. Mamba, *Ceram. Int.*, **50**, 29747 (2024); https://doi.org/10.1016/j.ceramint.2024.05.271
18. M. Hussain, M.E. El Sayed, M. Anwar, A. Samir, M.F. Warsi and Z.M. El-Bahy, *J. Alloys Compd.*, **1010**, 177242 (2025); https://doi.org/10.1016/j.jallcom.2024.177242
19. K. Islam, M. Haque, A. Kumar, A. Hoq, F. Hyder and S.M. Hoque, *Nanomaterials*, **10**, 2297 (2020); https://doi.org/10.3390/nano10112297
20. N. Masunga, O.K. Mmelesi, K.K. Kefeni and B.B. Mamba, *J. Environ. Chem. Eng.*, **7**, 103179 (2019); https://doi.org/10.1016/j.jece.2019.103179
21. N.S. Al-Bassami, *Ceram. Int.*, **50**, 26680 (2024); https://doi.org/10.1016/j.ceramint.2024.04.396
22. G. Vinod, K. Rajashekhar and J.L. Naik, *Ceram. Int.*, **49**, 2829 (2023); https://doi.org/10.1016/j.ceramint.2022.09.265
23. K.M.S. Katubi, H. Fatima, S. Siddique, Z.A. Alrowaili, M.S. Al-Buriahi, I. Shakir, M. Anwar and M.F. Warsi, *J. Inorg. Organomet. Polym. Mater.*, **35**, 5611 (2025); https://doi.org/10.1007/s10904-025-03611-z
24. K.R. Sanchez-Lievanos, J.L. Stair and K.E. Knowles, *Inorg. Chem.*, **60**, 4291 (2021); https://doi.org/10.1021/acs.inorgchem.1c00040
25. P. Thakur, R. Sharma, V. Sharma, P.B. Barman, M. Kumar, D. Barman, S.C. Katyal and P. Sharma, *J. Magn. Magn. Mater.*, **432**, 208 (2017); https://doi.org/10.1016/j.jmmm.2017.01.081
26. E. Martins, A.G. Jerônimo, R. Barbosa, L. Neves, E. Santos, T. Meira, J.A. Osajima, P. Trigueiro, A.S. Soares and R.R. Peña-Garcia, *Mater. Chem. Phys.*, **318**, 129300 (2024); https://doi.org/10.1016/j.matchemphys.2024.129300
27. P. Ramesh, G. Vinod, K. Rajashekhar, N.A. Elayah, A. Ramesh and J.L. Naik, *Appl. Phys., A Mater. Sci. Process.*, **130**, 687 (2024); https://doi.org/10.1007/s00339-024-07798-9

28. B. Zhou, Y.W. Zhang, C.S. Liao, C.H. Yan, L.Y. Chen and S.Y. Wang, *J. Magn. Magn. Mater.*, **280**, 327 (2004); https://doi.org/10.1016/j.jmmm.2004.03.031
29. M. Shkir, J. Hakami, M. Milon Hossain, N.S. Awwad and A. Khan, *Inorg. Chem. Commun.*, **140**, 109439 (2022); https://doi.org/10.1016/j.inoche.2022.109439
30. I. Malaescu, M. Poienar and C.N. Marin, *Crystals*, **15**, 184 (2025); https://doi.org/10.3390/cryst15020184
31. R. Rajesh Kanna, K. Sakthipandi, S.M.S.M.A. Maraikkayar, N. Lenin and M. Sivabharathy, *J. Rare Earths*, **36**, 1299 (2018); https://doi.org/10.1016/j.jre.2018.03.033
32. X. Qin, T. Zhang, J. Wang, R. Zhao, Y. Ma, F. Wang and X. Xu, *J. Alloys Compd.*, **929**, 167256 (2022); https://doi.org/10.1016/j.jallcom.2022.167256
33. A. Aslam, A.U. Rehman, N. Amin, M. Amami, M.A. Nabi, H. Alrobei, M. Asghar, N.A. Morley, M. Akhtar, M.I. Arshad, M. Maraj and K. Abbas, *J. Supercond. Nov. Magn.*, **35**, 473 (2022); https://doi.org/10.1007/s10948-021-06085-5
34. W. Zhang, X. Ye, D. Xu, C. Liu, D. Fang and B. Li, *Appl. Phys., A Mater. Sci. Process.*, **128**, 1 (2022); https://doi.org/10.1007/s00339-021-05118-z
35. R. Nivetha and A.N. Grace, *J. Alloys Compd.*, **796**, 185 (2019); https://doi.org/10.1016/j.jallcom.2019.05.021
36. Z. Latif, A.U. Rehman, N. Amin, M.I. Arshad and R. Marzouki, *RSC Adv.*, **13**, 34308 (2023); https://doi.org/10.1039/D3RA02080K
37. L.G. Sun, G. Wu, Q. Wang and J. Lu, *Mater. Today*, **38**, 114 (2020); https://doi.org/10.1016/j.mattod.2020.04.005
38. B. Pandey, R.C. Srivastava, C.S. Joshi and H.K. Verma, *Physica B*, **711**, 417302 (2025); https://doi.org/10.1016/j.physb.2025.417302
39. P. Rani, E. Jyothirmai, V. Ludhiya, K. Venu Prasad, J. Pandari and V. Nathanial, *Mater. Chem. Phys.: Sustain. Energy*, **2**, 100004 (2025); https://doi.org/10.1016/j.macse.2024.100004
40. J. Li, M. Yousaf, Q. Hayat, M. Akbar, A. Noor, M.A.K.Y. Shah, F. Qi and Y. Lu, *J. Rare Earths*, **41**, 1746 (2023); https://doi.org/10.1016/j.jre.2022.12.007
41. M. Khosravi, S. Sharafi and A. Irannejad, *Appl. Phys., A Mater. Sci. Process.*, **130**, 335 (2024); https://doi.org/10.1007/s00339-024-07507-6
42. G. Satayanarayana Goud, N. Venkatesh, D. Ravi Kumar, S. Ismail Ahmad and P. Veerasomaiah, *ECS J. Solid State Sci. Technol.*, **13**, 073005 (2024); https://doi.org/10.1149/2162-8777/ad5dfb
43. R. Jasrotia, N. Kumari, R. Verma, S.K. Suman, S.K. Godara, J. Ahmed, S.M. Alshehri, B. Pandit, S. Kumar, Himanshi, S. Sharma, Kirti and P.K. Maji, *J. Rare Earths*, **41**, 1763 (2023); https://doi.org/10.1016/j.jre.2022.08.015
44. G. Vinod, K. Rajashekhar, Y. Sandeep and J. Laxman Naik, *J. Magn. Magn. Mater.*, **562**, 169772 (2022); https://doi.org/10.1016/j.jmmm.2022.169772
45. G. Vinod, K. Rajashekhar, N.A. Elayah, K. Ganga Reddy, A. Ramesh, P. Ramesh and J. Laxman Naik, *Inorg. Chem. Commun.*, **159**, 111817 (2024); https://doi.org/10.1016/j.inoche.2023.111817
46. T. Tatarchuk, M. Bououdina, W. Macyk, O. Shyichuk, N. Paliychuk, I. Yaremiy, B. Al-Najar and M. Pacia, *Nanoscale Res. Lett.*, **12**, 141 (2017); https://doi.org/10.1186/s11671-017-1899-x
47. A.A. Ibiyemi, G.T. Yusuf, O. Olubosede, A. Olusola and H.A. Akande, *Phys. Scr.*, **97**, 025804 (2022); https://doi.org/10.1088/1402-4896/ac4a95
48. S.B. Somvanshi, S.A. Jadhav, M.V. Khedkar, P.B. Kharat, S.D. More and K.M. Jadhav, *Ceram. Int.*, **46**, 13170 (2020); https://doi.org/10.1016/j.ceramint.2020.02.091
49. U. Dhasharatha, G. Vinod, K. Rajashekhar, D. Mallesh, B. Sreematha and J. Laxman Naik, *Ceram. Int.*, **50**, 46940 (2024); https://doi.org/10.1016/j.ceramint.2024.09.046
50. M. Akhter, M.K. Amin, P.K. Dhar, S.K. Dey, M.S. Hossain and S.K. Dutta, *RSC Adv.*, **14**, 29083 (2024); https://doi.org/10.1039/D4RA04334K